

# ***Ab initio* Study of High-field Transport in Low Symmetry Crystals —Velocity-Field Curves in Monoclinic $\beta$ -Ga<sub>2</sub>O<sub>3</sub>**

Krishnendu Ghosh<sup>†</sup> and Uttam Singiseti<sup>§</sup>

Electrical Engineering Department, University at Buffalo, Buffalo NY 14260

<sup>†</sup>kghosh3@buffalo.edu, <sup>§</sup>uttamsin@buffalo.edu

**Abstract:** We study the high-field transport in a low symmetry crystal using *ab initio* electron phonon interaction (EPI) elements in a full band Monte Carlo (FBMC) simulation. Scattering rate calculation and the final state selection in the FBMC simulation use complete wave-vector (both electron and phonon) and crystal direction dependent EPI elements. We propose and evaluate a ‘semi-coarse’ version of the Wannier-Fourier interpolation method [F. Giustino, M. L. Cohen, and S. G. Louie, Physical Review B, vol. 76, no. 16, 2007] for short-range EPI elements in order to ease the computational requirement in FBMC simulation. During the interpolation of the EPI, the inverse Fourier sum over the real-space electronic grids is done on a coarse mesh while the unitary rotations are done on a fine mesh. The FBMC simulation probes the anisotropy in transport not just with the band-structure also with the *ab initio* EPI elements. High field transport in monoclinic  $\beta$ -Ga<sub>2</sub>O<sub>3</sub> is studied for the first time with deep insight on the contribution of different phonon modes, relative emission rates of different modes, and velocity field characteristics for electric fields ranging up to 450 kV/cm in different crystal orientations. This work provides the first report on velocity-field curves in  $\beta$ -Ga<sub>2</sub>O<sub>3</sub>. A peak velocity of  $\approx 2 \times 10^7$  cm/s is estimated at an electric field of 200 kV/cm.

Electron phonon interactions (EPIs) play an important role in diverse fields. Traditionally they were modelled using phenomenological deformation potentials that could explain the experimental results. However, such approach ignores complex issues such as anisotropy and also requires experimental data to set the phenomenological constants. With the expanding search for new materials, revealing the right physics of EPI is crucial to engineer the electron and phonon dynamics. High-field electron transport is important not just for electronics, also for several branches of photonics. Hence it is important to have a clear quantitative understanding of how EPIs affect high field electron transport. There have been several studies on estimating complete *ab initio* scattering rates in recent years [1–5] and also on determining low-field electron mobility using them [2, 5]. These studies are primarily done on material systems with fairly high symmetry. Low symmetry materials pose several challenges in *ab initio* transport calculations including a larger irreducible Brillouin zone, low degeneracy of phonon modes and EPI elements, and the crystal orientation dependence of the long-range EPI and the dielectric tensor. Here, we systematically study the physics of EPI in a low symmetry material and also reveal how they affect the electron transport keeping in focus the computational challenges. Monoclinic  $\beta$ -Ga<sub>2</sub>O<sub>3</sub> has a large primitive cell with low crystal symmetry which makes it an ideal benchmark system to study electron transport from first principles. Besides,  $\beta$ -Ga<sub>2</sub>O<sub>3</sub> is an emerging wide-bandgap material with excellent potential for power electronics applications. Experimentally demonstrated high breakdown voltage makes it an attractive material for next generation power electronics [6–10] in addition to deep UV optoelectronic applications [11, 12]. However, the low symmetry monoclinic structure and large primitive cell present challenges to accurate prediction of optical, and electrical transport properties. There have been a number of reports on thermal, dielectric, and optical properties of this material [13–20]. Recently, we reported low field mobility calculation in this material from first principles [21] that fairly agreed with experimental report [22]. However, there is no report on the high field transport properties on this material. In this work, we report the investigation of the high-field transport in  $\beta$ -Ga<sub>2</sub>O<sub>3</sub> through a full band Monte Carlo (FBMC) calculation incorporating electron phonon interactions calculated from first principles. We first discuss our entire computational strategy and then move on to discuss the results obtained for  $\beta$ -Ga<sub>2</sub>O<sub>3</sub>.

Fig.1 shows an overview of the calculation. In the following we refer to electron and phonon wave-vectors as  $\mathbf{k}$  and  $\mathbf{q}$  respectively. The calculation begins with self-consistent field calculation on equilibrium lattice structure followed by the extraction of Kohn-Sham(KS) eigen values. Next, lattice response calculations are done based on the density functional perturbation theory (DFPT) [23]. This provides the dynamical phonon matrix and also the perturbation in the self-consistent potential for each perturbation. Diagonalizing the dynam-

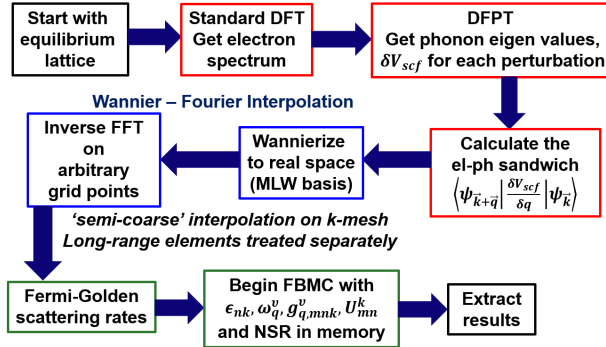


Figure 1: The calculation flowchart to obtain transport properties from first-principles. The red outlines indicate calculations on coarse  $\mathbf{k}$  and  $\mathbf{q}$  meshes while the green outlines indicate calculations on a fine mesh. Wannier Fourier interpolation steps are indicated with blue outlines. A ‘semi-coarse’  $\mathbf{k}$ -mesh interpolation strategy is utilized for the first time to interpolate the short-range matrix elements (see main text for the details). The FBMC algorithm needs the electron spectrum ( $\epsilon_{n\mathbf{k}}$ ), phonon spectrum ( $\omega_{\mathbf{q}}^{\nu}$ ), EPI elements ( $g_{\mathbf{q},m\mathbf{n}\mathbf{k}}^{\nu}$ ), rotation matrices ( $U_{mn}^{\mathbf{k}}$ ), and the normalized scattering rates(NSR) to be stored in the memory.

ical phonon matrix gives the phonon eigen values and the EPI elements are computed from the perturbation in the self-consistent potential. These are done on a coarse mesh due to the heavy computational requirement of DFPT. However, convergence in the scattering rates calculation requires fine resolution in the matrix elements. Hence the dynamical matrices and the EPI elements need to be interpolated on a fine mesh. This interpolation is done using a Wannier-Fourier interpolation scheme [24] that utilizes crystal periodicity to transform the reciprocal space matrix elements to real space using maximally localized Wannier functions (MLWFs) and then inverse Fourier transform to arbitrary points on reciprocal space. However, the long-range polar coupling needs a separate treatment due to its divergence near the zone center. Recent formulation [25] on long-range EPI interpolation scheme is used to interpolate the long range elements. Screening of the long-range elements is employed using a generalized Lyddane-Sachs-Teller relation which is found to be appropriate for monoclinic materials [15]. We assume that a given mode can only be screened by modes with higher energies.

Next we describe the interpolation method used for the short-range non-polar EPI elements. The fine resolution needed on both  $\mathbf{k}$  and  $\mathbf{q}$  meshes requires large memory requirement in computations which becomes an even more serious problem for materials with many phonon modes such as  $\beta$ -Ga<sub>2</sub>O<sub>3</sub>. Unlike scattering rate calculations, an ‘on the fly’ method [1, 26] could not be used in the FBMC calculation since we need to use the matrix elements for final state selection as well. An ‘on the fly’ calculation inside the final state selection process is inefficient since the summation over the real-space grid has to be per-

formed for each electron, each time interval, and each scattering process making it extremely slow. Hence the fine grid matrix elements need to be stored in the memory. Here we describe a method that is computationally efficient with small sacrifice in accuracy. Using the definitions of electronic Wannier functions(WF) [24], we write the short range non-polar EPI matrix elements on a fine  $\mathbf{k}$  and  $\mathbf{q}$  meshes as –

$$g_{short}^{\nu}(\mathbf{k}, \mathbf{q}) = \frac{1}{N_e^2} \sum_{\mathbf{R}_e, \mathbf{R}'_e} U_{\mathbf{k}+\mathbf{q}} \left[ e^{i\mathbf{k}\cdot(\mathbf{R}_e-\mathbf{R}'_e)} g_{short}^{\nu}(\mathbf{R}_e - \mathbf{R}'_e, \mathbf{q}) \right] U_{\mathbf{k}}^{\dagger} \quad (1)$$

Here, the unitary rotation matrices  $U$  have a dimension of  $N^w \times N^w$ , where  $N^w$  is the size of the Wannier subspace.  $g_{short}^{\nu}(\mathbf{k}, \mathbf{q})$  is the short-range EPI on both fine meshes.  $\mathbf{R}_e$  is the center of an unit cell in the supercell and  $N_e$  is the total number of unit cells in the supercell. Eq.1 shows the inverse Fourier transform of the real-space (on electronic mesh)  $g_{short}^{\nu}(\mathbf{R}_e - \mathbf{R}'_e)$  to an arbitrary  $\mathbf{k}$ -point while the  $\mathbf{q}$ -mesh interpolated information is already present on the right-hand side of the equation. The total memory requirement to store the short range EPI on both fine meshes would be governed by  $N^k \times N^{\nu} \times N^q \times N^{w2}$ , which becomes large for the required  $N^k$  and  $N^q$  where  $N^k$ ,  $N^q$  and  $N^{\nu}$  are the size of the fine  $\mathbf{k}$ -mesh, fine  $\mathbf{q}$ -mesh, and the number of phonon modes respectively. For this work the corresponding memory requirement becomes more than 500 terabytes. Hence, we propose a way to circumvent the problem. The primary contribution to  $g_{short}^{\nu}(\mathbf{R}_e - \mathbf{R}'_e, \mathbf{q})$  comes when the two involved electronic WFs are on the same unit cell since the overlap of remote WFs are low (although not negligible and we discuss that later) in case of MLWFs. Under such condition we can rewrite (after simple algebraic manipulation) Eq.1 as –

$$g_{short}^{\nu,0}(\mathbf{k}, \mathbf{q}) = \frac{1}{N_e} U_{\mathbf{k}+\mathbf{q}} g_{short}^{\nu}(\mathbf{0}_e, \mathbf{q}) U_{\mathbf{k}}^{\dagger} = \frac{1}{N_e} U_{\mathbf{k}+\mathbf{q}} U_{\mathbf{k}_c+\mathbf{q}}^{\dagger} g_{short}^{\nu,0}(\mathbf{k}_c, \mathbf{q}) U_{\mathbf{k}_c} U_{\mathbf{k}}^{\dagger} \quad (2)$$

Hence the same unit cell contribution  $g_{short}^{\nu,0}(\mathbf{k}, \mathbf{q})$  can be accessed just by storing  $g_{short}^{\nu,0}(\mathbf{k}_c, \mathbf{q})$  on a coarse  $\mathbf{k}$ -mesh( $\mathbf{k}_c$ ) and the rotation matrices. This reduces the memory requirement by several orders. Next, we discuss the contribution from remote WFs. Now we consider Eq.1 with  $\mathbf{R}_e \neq \mathbf{R}'_e$ . Under such conditions, a reduction similar to Eq.2 would have been perfectly possible if the phase factor  $e^{i\mathbf{k}\cdot(\mathbf{R}_e-\mathbf{R}'_e)}$  was absent. But note that the  $\mathbf{k}$ -space smoothness of the matrix elements in Wannier gauge makes the contribution from the remote unit cells much smaller compared to the same unit cell. Under such argument, treating the remote WF contribution similar to Eq.2 introduces small inaccuracy in calculation but eases the computational requirement to a great extent. So the overall  $g_{short}^{\nu}(\mathbf{k}, \mathbf{q})$  can be obtained from  $g_{short}^{\nu}(\mathbf{k}_c, \mathbf{q})$  and the rotation matrices on the fine mesh. The essential idea is to rotate the coarse-mesh elements to an optimal Bloch-space (that produces the MLWFs), perform

Fourier transform to real space followed by inverse Fourier transform on another coarse  $\mathbf{k}$ -mesh ( $\mathbf{k}_c$ , if  $\mathbf{k}_c$  is same as the DFT coarse mesh, the two transforms are not required). The fine  $\mathbf{k}$ -mesh elements could be obtained ‘on the fly’ just by un-rotating the elements back to the normal Bloch-space using the fine  $\mathbf{k}$ -mesh rotation matrices. This reduces the ‘on the fly’ time consumed in converting the elements back and forth between reciprocal and real spaces while at the same time mitigating the huge memory requirement for storing the elements on both fine  $\mathbf{k}$  and  $\mathbf{q}$  meshes. We first propose this strategy here and refer to this type of  $\mathbf{k}$ -mesh sampling as a ‘semi-coarse’ sampling since the unitary rotations are on fine mesh but the inverse Fourier transform sum is on a coarse mesh. The corresponding interpolation results using this method for  $\beta$ -Ga<sub>2</sub>O<sub>3</sub> is shown and compared with a regular fine  $\mathbf{k}$ -mesh interpolation later. It is important to mention here that this sacrifice of accuracy does not lead to any sacrifice of the crystal symmetry mediated selection rules of non-polar scattering since that is taken care of inside  $g'_{short}(\mathbf{R}_e - \mathbf{R}'_e, \mathbf{q})$ .

Low field transport calculations based on Boltzmann transport formalism can be carried out using the relaxation time approximation or more rigorous iterative techniques [27]. However, high-field transport requires extensive Monte Carlo simulations. We begin with *ab initio* KS eigen values on a fine reciprocal  $\mathbf{k}$ -mesh, phonon eigen values (on two different types of  $\mathbf{q}$ -meshes—one for short-range elements that span the entire BZ, while the other for the long range elements which exist only in the vicinity of the zone center), both long-range and short range EPIs, and scattering rates on the fine  $\mathbf{k}$ -mesh with contributions from the different phonon modes being separated. The scattering rates from a given  $\mathbf{k}$  point is normalized using the running sum of all the possible mechanisms (absorption/emission, polar/non polar, intra-band/inter-band for each mode) allowed from that point. The normalized scattering rates (NSR) are stored in a look-up table whose memory requirement scales as  $N^w \times N^m$ , where  $N^m$  is the total number of scattering mechanisms.  $N^m$  consists of different phonon modes each with different possible scattering flavors—absorption/emission, polar/non-polar, and intraband/interband. It is noted that for polar scattering we do not consider any inter-band transitions since the overlap of the electronic phases from different bands vanish under  $\mathbf{q} \rightarrow 0$  limit. So, for  $\beta$ -Ga<sub>2</sub>O<sub>3</sub>, 30 phonon modes give  $N^m = 180$ . The large memory requirement of the NSR is met by using a hybrid parallelization scheme on the FBMC algorithm where the NSR are stored on shared memory windows [28] available to all processes running under the same computing node. These NSR are used to build the electron trajectories in the reciprocal space. Self-scattering mechanism [29, 30] is included so that the final results are independent of the duration of the small time intervals that make up the entire FBMC time span. In the following we discuss the results of the calculations done on  $\beta$ -Ga<sub>2</sub>O<sub>3</sub>.

Standard DFT calculations are done on  $\beta$ -Ga<sub>2</sub>O<sub>3</sub> primitive unit cell with norm-conserving

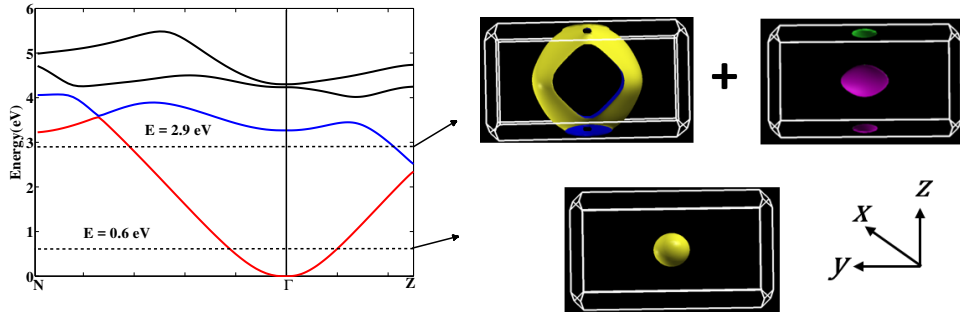


Figure 2: The DFT calculated conduction band energies are shown for  $\beta$ -Ga<sub>2</sub>O<sub>3</sub>. The first two bands (shown in red and blue) are used in the transport calculation. On the right side the equi-energy surfaces (visualized by XCrySDen [31]) are shown for two different energies. It is evident that at lower energy the surface is spherically symmetric while higher energy introduces band anisotropy and also multiple bands.

pseudopotentials [32] on Ga and O using the Quantum ESPRESSO (QE) [33]. Semi-core  $d$  orbitals on Ga are taken as valence states. A  $8 \times 8 \times 4$  Monkhorst-Pack [34] grid is used to sample the BZ and a 100 Ry plane wave cut-off energy is used for truncating reciprocal vectors. In Fig. 2 we show the resulting KS eigen values along two reciprocal vectors. 4 conduction states are shown out of which first two are used in subsequent transport calculations. Also in Fig. 2 the equi-energy surfaces are shown for two different energies. It can be seen that at a lower energy the surface is spherically symmetric, while at higher energies the surface becomes anisotropic and also contributions from higher energy bands cannot be neglected. We interpolated the KS Hamiltonian through MLWFs by using the wannier90 code [35]. Our optimal Wannier subspace (S) consists of two low lying conduction bands within a frozen energy window. Atom centered  $s$  orbitals as an initial guess produced a gauge invariant spread of  $20.33 \text{ \AA}^2$  and gauge dependent spreads of  $5.91 \text{ \AA}^2$  and  $2.88 \text{ \AA}^2$  (diagonal and off-diagonal respectively). We consider these numbers to be good enough in terms of spread minimization since the entire S consists of anti-bonding states and the bottom of the conduction band is of delocalized  $s$  character unlike the valence states which are dominated primarily by O  $2p$  states and Ga  $3d$  states. The phonon calculation is done under DFPT using QE with a  $4 \times 4 \times 4$   $\mathbf{q}$ -mesh. The phonon eigen values and the short-range EPI matrix elements are interpolated on a fine  $\mathbf{q}$ -mesh ( $64 \times 64 \times 32$  spanning the entire BZ) using a modified version of the EPW code [26]. The long-range interaction is calculated separately using the Born-effective charge tensor and the phonon displacement patterns on a  $64 \times 64 \times 32$  mesh spanning 0.2 times the reciprocal vectors surrounding the  $\Gamma$  point. Scattering rates are calculated using Fermi Golden rule with a Lorentzian smearing of the energy conserving delta function to obtain the scattering rates on a fine BZ mesh within an energy window of 3.4 eV.

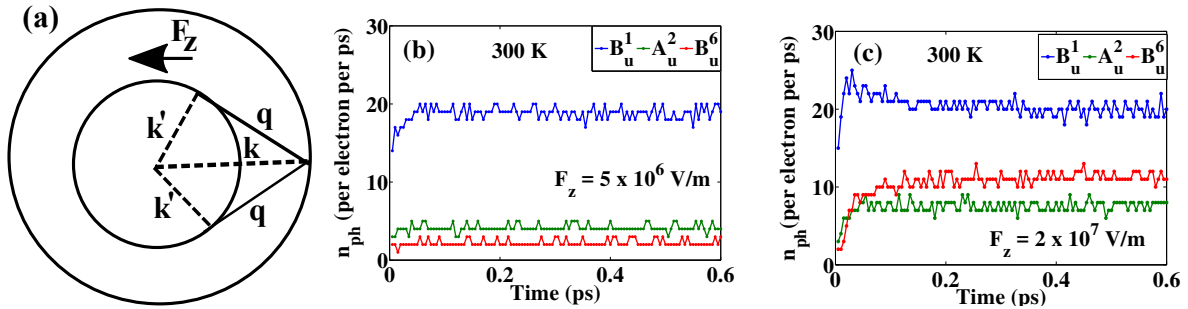


Figure 3: (a) The available electronic phase space after a long-range scattering of low-energy electrons requires the phonon wave-vector to be inclined towards a direction opposite to the electron wave-vector. (b-c) The emission rate of the three different LO modes for electric fields applied along the  $z$  direction. The  $A_u$  mode being polarized orthogonal to the applied field direction does not show an increase in emission rate in spite of an increase in the electric field strength.

The choice of such window makes sure only two electronic bands are required to be taken. Next we discuss on the effects of the EPI on different regimes of transport in  $\beta$ - $\text{Ga}_2\text{O}_3$ .

Polar crystals usually have their low-field electron mobility dominated by the long-range polar EPI.  $\beta$ - $\text{Ga}_2\text{O}_3$  is not an exception as was revealed in our previous work [21]. Before discussing the high field transport, we explore the anisotropy in the low field electron mobility. Recent experiments have demonstrated [36] a small (10%-15%) anisotropy in mobility although the energy band near the  $\Gamma$  point is fairly isotropic [37]. The obvious question that arises is —what is the origin of this anisotropy in mobility? The answer lies in the anisotropy in the long-range polar optical EPI which was calculated in our previous work [21]. Here through Monte Carlo calculation we show the anisotropy in low field electron transport. However, intuitively, the underlying idea is that an electron drifting along a certain direction gets scattered more by modes whose coupling strength projected along that direction is higher. As a result the mobility along that direction gets lowered. We show this idea schematically in Fig. 3(a) where the electron energy is comparable with the phonon energy. If the electron is propagating along  $z$  direction, the available phase space after a phonon emission allows  $\mathbf{q}$  vectors that are more inclined in the  $z$  direction and this becomes more prominent with decreasing electron energy. In case of  $\beta$ - $\text{Ga}_2\text{O}_3$  the dominant  $B_u$  mode that controls the low-field mobility is polarized along the  $z$  direction [21] and hence in the light of the above argument the mobility is expected to be lower in that direction as is observed in experiments [36]. In Fig. 3(b) and 3(c) we verify this through Monte Carlo study of the emission rates of three different phonons ( $B_u^1=21.3$  meV,  $A_u^2=36.3$  meV, and  $B_u^6=70.2$  meV) at different electric fields. Under a relatively low electric field applied along  $z$  direction, the emission rate for the  $B_u^1$  mode is higher compared to the other two modes implying that

the electron energy is not high enough to emit higher energy modes. However, as we increase the field strength along the same direction, we find that the emission rate for  $B_u^6$  increases while  $A_u^2$  still remains lower. This is because the  $A_u^2$  mode is polarized along the  $y$  direction and unable to couple strongly with electrons drifting along the  $z$  direction.

Next, we discuss the short-range non-polar EPI elements that are primarily responsible for higher momentum and energy relaxation rates at high fields that lead to saturation in velocity. The Wannier-Fourier interpolated short-range matrix elements are shown in Fig. 4(a) (blue curve). We show the sum of the squared magnitude of the coupling over all the vibrational modes. The long-range polar coupling is also shown (red curves) on the same plot for comparison. The  $\mathbf{q}$  dependence of  $\sum_\nu |g_{short}^\nu|^2$  is to be noted along with its crystal direction dependence ( $\Gamma$ -Z and  $\Gamma$ -N). The inset shows a contour plot on the 2D plane formed by the same two directions. The symmetry of the short-range element observed on the contour plot is a signature of the inversion symmetry associated with the  $C_{2m}$  space group of a monoclinic crystal. On Fig. 4(b) we show a mode wise splitting of the short-range contribution for two different  $\mathbf{q}$  vectors. The red bar plots show  $|g_{short}^\nu|^2$  for initial electron wave-vector  $\mathbf{k}$  at  $0.25 \times \Gamma Z$  away from  $\Gamma$  while the phonon wave-vector  $0.5 \times \Gamma Z$  away from  $\Gamma$ . The corresponding two points from the green bar plots are  $0.125 \times \Gamma N$  away from  $\Gamma$  and  $0.25 \times \Gamma N$  away from  $\Gamma$ . The reason for choosing such wave-vectors, as explained below, is to reflect the contribution of the individual phonon modes when maximum momentum relaxation can occur. The inset of Fig. 4(b) shows the scattering schematic for high energy electrons. It is assumed that the phonon mediated scattering of high energy ( $>2$  eV) electrons is elastic for the sake of better visualization in the inset. The long arrows correspond to a direction reversal of an electron which provides a high momentum relaxation. Unlike the low energy electron case, the available phase space allows phonon wave-vectors from all directions. But the higher momentum relaxing phonon wave-vectors need to be inclined as much opposite as possible to the propagating electron wave-vector. This explains the choice of electron and phonon wave-vectors to show the individual mode contributions in Fig.4(b). Now we discuss the results of the ‘semi-coarse’ sampling technique proposed for the interpolation of the short range EPI earlier. Fig. 4(c) shows the short range EPI element along the  $\Gamma$ -Z- $\Gamma$  direction. The  $\mathbf{q}$  vector is kept fixed at halfway along the  $\Gamma Z$ . The DFPT calculated coarse-mesh element is shown with red dots while a regular fine mesh interpolated result is shown with red solid curve. As expected, we see that as we increase the resolution of the semi-coarse  $\mathbf{k}$ -mesh, the interpolation approaches closer to the red solid curve. The kinks on the semi-coarse curves occur when the representative coarse  $\mathbf{k}$ -mesh point corresponding to a fine- $\mathbf{k}$  mesh point changes. The small errors incurred due to this strategy is acceptable given the resulting ease in computational memory requirement.

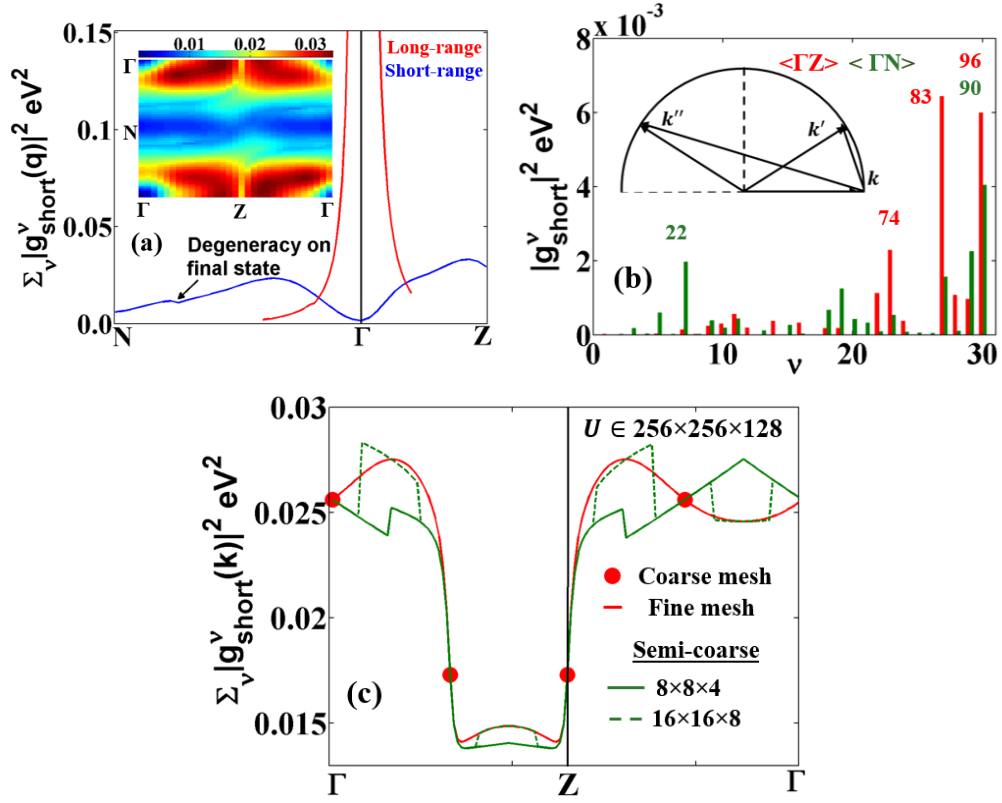


Figure 4: (a) The dependence of the EPI elements with the phonon wave-vector. The inset shows a contour plot of the short-range EPI on the  $\Gamma$ Z- $\Gamma$ N plane. The initial electronic state is taken at the  $\Gamma$  and hence the inversion symmetry of the crystal is reflected in the contour plot (see main text for details). The small discontinuity on the short-range EPI marked by the arrow is a result of the gauge ambiguity arising from degenerate final electronic states (see Fig 2). Such discontinuity does not affect the total scattering rate since the latter is gauge-invariant. (b) The mode-wise splitting of the short-range EPI along for two  $\mathbf{q}$  points in two different directions. The phonon energies (meV) for the dominating modes are shown with corresponding colors. (Inset) At higher electron energies a high momentum relaxation requires phonon wave-vectors that are inclined towards opposite direction of the electronic wave-vector. (c) The interpolated elements in  $\mathbf{k}$ -space using the semi-coarse  $\mathbf{k}$ -mesh strategy. The  $\mathbf{q}$  point is kept fixed at a point halfway along  $\Gamma$ Z. A pure fine-mesh interpolation is also shown for comparison. The maximum observed deviation between the  $8 \times 8 \times 4$  ‘semi-coarse’ mesh and the fine mesh elements is  $\approx 10\%$ - $12\%$ . In (a-c) the initial and final electronic band indices are taken to be the first band.

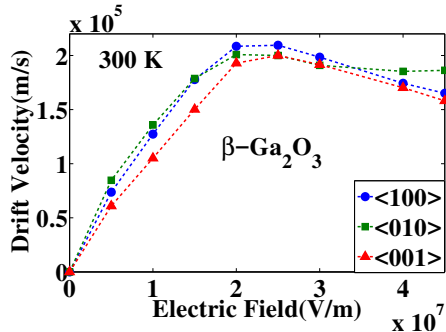


Figure 5: Velocity-field characteristic of  $\beta$ -Ga<sub>2</sub>O<sub>3</sub> at room temperature in three different directions

Fig. 5 shows the velocity-field curves in three different Cartesian directions calculated from FBMC using the scattering strengths discussed in the previous sections. We see that the velocity increases in all three directions up to 200 kV/cm. The difference in initial slope of the velocity is due to the small anisotropy in low field mobility while the small anisotropy beyond 200 kV/cm is explained below. We note that the negative differential mobility is less than that in materials like GaAs since the electronic satellite valleys (Fig. 2) occur at a much higher energy (the lowest one being at  $\approx 2.4$  eV) compared to that in GaAs ( $\approx 0.3$  eV). The high field velocity is relatively higher in the  $y$  direction. We attribute this to two facts—the slope of the energy band drops at a higher  $\mathbf{k}$  compared to the other two directions and the dominating high energy non-polar (along  $\Gamma N$  which is inclined towards the Cartesian  $y$  direction) phonon (90 meV) is weaker compared to the modes (96 meV and 83 meV) in Cartesian  $z$  direction (same as  $\Gamma Z$ ) leading to less energy relaxation along  $y$  direction. The average peak velocity is  $\approx 2 \times 10^7$  cm/s at an electric field of 200 kV/cm. For comparison, the average saturation velocity is slightly lower than wurzite GaN [38] apparently due to a lower gradient of the energy bands. As mentioned before, we took into account two electronic bands. Considering more electronic bands and a higher energy window might produce more accurate results but we believe that will not alter the trend in the anisotropy.

In summary, we have highlighted the role of full-band EPI in controlling the electron transport. A ‘semi-coarse’  $\mathbf{k}$ -mesh version of the Wannier-Fourier interpolation [24] strategy is proposed for the short-range EPI in order to make it computationally tractable for materials with many phonon modes and low crystal symmetry. The calculated EPIs are used in an FBMC algorithm to analyze effects of multiple phonons in high-field transport. Monoclinic  $\beta$ -Ga<sub>2</sub>O<sub>3</sub> is studied under this theoretical manifold followed by the prediction of the velocity-field characteristics. A (10%-15%) anisotropy in low-field mobility and a peak velocity of  $\approx 2 \times 10^7$  cm/s at a critical electric field ( $E_c$ ) of 200 kV/cm in three different directions are estimated. Transport anisotropy beyond  $E_c$  is found to be a joint effect of band-structure

and anisotropic EPI.

The authors acknowledge the support from the National Science Foundation (NSF) grant (ECCS 1607833). The authors also acknowledge the excellent high performance computing cluster provided by the Center for Computational Research (CCR) at the University at Buffalo.

## References

- [1] M. Bernardi, D. Vigil-Fowler, C. S. Ong, J. B. Neaton, and S. G. Louie, “Ab initio study of hot electrons in GaAs,” *Proc Natl Acad Sci USA*, vol. 112, no. 17, pp. 5291–6, 2015.
- [2] J. Zhou and M. Bernardi, “Ab initio electron mobility and polar phonon scattering in GaAs,” *arXiv preprint arXiv:1608.03514*, 2016.
- [3] M. Bernardi, D. Vigil-Fowler, J. Lischner, J. B. Neaton, and S. G. Louie, “Ab initio study of hot carriers in the first picosecond after sunlight absorption in silicon,” *Phys Rev Lett*, vol. 112, no. 25, p. 257402, 2014.
- [4] J. Zhou, B. Liao, and G. Chen, “First-principles calculations of thermal, electrical, and thermoelectric transport properties of semiconductors,” *Semiconductor Science and Technology*, vol. 31, no. 4, p. 043001, 2016.
- [5] J. Sjakste, N. Vast, M. Calandra, and F. Mauri, “Wannier interpolation of the electron-phonon matrix elements in polar semiconductors: Polar-optical coupling in GaAs,” *Physical Review B*, vol. 92, no. 5, 2015.
- [6] M. Higashiwaki, K. Sasaki, T. Kamimura, M. Hoi Wong, D. Krishnamurthy, A. Kuramata, T. Masui, and S. Yamakoshi, “Depletion-mode Ga<sub>2</sub>O<sub>3</sub> metal-oxide-semiconductor field-effect transistors on  $\beta$ -Ga<sub>2</sub>O<sub>3</sub> (010) substrates and temperature dependence of their device characteristics,” *Applied Physics Letters*, vol. 103, no. 12, p. 123511, 2013.
- [7] M. Higashiwaki, K. Sasaki, A. Kuramata, T. Masui, and S. Yamakoshi, “Gallium oxide (Ga<sub>2</sub>O<sub>3</sub>) metal-semiconductor field-effect transistors on single-crystal  $\beta$ -Ga<sub>2</sub>O<sub>3</sub> (010) substrates,” *Applied Physics Letters*, vol. 100, no. 1, p. 013504, 2012.
- [8] T. Oishi, Y. Koga, K. Harada, and M. Kasu, “High-mobility  $\beta$ -Ga<sub>2</sub>O<sub>3</sub>  $\bar{2}01$  single crystals grown by edge-defined film-fed growth method and their schottky barrier diodes with ni contact,” *Applied Physics Express*, vol. 8, no. 3, p. 031101, 2016.
- [9] K. Sasaki, M. Higashiwaki, A. Kuramata, T. Masui, and S. Yamakoshi, “Schottky barrier diodes fabricated by using single-crystal  $\beta$ -Ga<sub>2</sub>O<sub>3</sub> (010) substrates,” *IEEE electron device letters*, vol. 34, no. 4, pp. 493–495, 2013.
- [10] K. Zeng, K. Sasaki, A. Kuramata, T. Masui, and U. Singisetti, “Depletion and enhancement mode  $\beta$ -Ga<sub>2</sub>O<sub>3</sub> MOSFETs with ALD SiO<sub>2</sub> gate and near 400 v breakdown

- voltage,” in *Device Research Conference (DRC), 2016 74th Annual*. IEEE, 2016, pp. 1–2.
- [11] S. Nakagomi, T. Momo, S. Takahashi, and Y. Kokubun, “Deep ultraviolet photodiodes based on  $\beta$ -Ga<sub>2</sub>O<sub>3</sub>/sic heterojunction,” *Applied Physics Letters*, vol. 103, no. 7, p. 072105, 2013.
- [12] T. Oshima, T. Okuno, N. Arai, N. Suzuki, S. Ohira, and S. Fujita, “Vertical solar-blind deep-ultraviolet schottky photodetectors based on  $\beta$ -Ga<sub>2</sub>O<sub>3</sub> substrates,” *Applied physics express*, vol. 1, no. 1, p. 011202, 2008.
- [13] B. Liu, M. Gu, and X. Liu, “Lattice dynamical, dielectric, and thermodynamic properties of  $\beta$ -Ga<sub>2</sub>O<sub>3</sub> from first principles,” *Applied Physics Letters*, vol. 91, no. 17, p. 172102, 2007.
- [14] Z. Guo, A. Verma, X. Wu, F. Sun, A. Hickman, T. Masui, A. Kuramata, M. Higashiwaki, D. Jena, and T. Luo, “Anisotropic thermal conductivity in single crystal  $\beta$ -gallium oxide,” *Applied Physics Letters*, vol. 106, no. 11, p. 111909, 2015.
- [15] M. Schubert, R. Korlacki, S. Knight, T. Hofmann, S. Schöche, V. Darakchieva, E. Janzén, B. Monemar, D. Gogova, Q. T. Thieu, R. Togashi, H. Murakami, Y. Kumagai, K. Goto, A. Kuramata, S. Yamakoshi, and M. Higashiwaki, “Anisotropy, phonon modes, and free charge carrier parameters in monoclinic  $\beta$ -gallium oxide single crystals,” *Physical Review B*, vol. 93, no. 12, 2016.
- [16] Y. Zhang, J. Yan, G. Zhao, and W. Xie, “First-principles study on electronic structure and optical properties of Sn-doped  $\beta$ -Ga<sub>2</sub>O<sub>3</sub>,” *Physica B: Condensed Matter*, vol. 405, no. 18, pp. 3899–3903, 2010.
- [17] S. Badescu, D. Thomson, J. Mann, and G. Jessen, “Atomistic modelling for predicting  $\beta$ -gallium oxide properties,” 2015, presented at The 1st International Workshop on Gallium Oxide and Related Materials, Kyoto University, Kyoto, Japan.
- [18] M. Schubert, “Coordinate-invariant lyddane-sachs-teller relationship for polar vibrations in materials with monoclinic and triclinic crystal systems,” *Physical Review Letters*, vol. 117, no. 21, p. 215502, 2016.
- [19] F. Ricci, F. Boschi, A. Baraldi, A. Filippetti, M. Higashiwaki, A. Kuramata, V. Fiorentini, and R. Fornari, “Theoretical and experimental investigation of optical absorption anisotropy in  $\beta$ -Ga<sub>2</sub>O<sub>3</sub>,” *Journal of Physics: Condensed Matter*, vol. 28, no. 22, p. 224005, 2016.
- [20] K. A. Mengle, G. Shi, D. Bayerl, and E. Kioupakis, “First-principles calculations of the near-edge optical properties of  $\beta$ -Ga<sub>2</sub>O<sub>3</sub>,” *Applied Physics Letters*, vol. 109, no. 21, p. 212104, 2016.

- [21] K. Ghosh and U. Singiseti, “Ab initio calculation of electron–phonon coupling in monoclinic  $\beta$ -Ga<sub>2</sub>O<sub>3</sub> crystal,” *Applied Physics Letters*, vol. 109, no. 7, p. 072102, 2016.
- [22] A. Parisini and R. Fornari, “Analysis of the scattering mechanisms controlling electron mobility in  $\beta$ -Ga<sub>2</sub>O<sub>3</sub> crystals,” *Semiconductor Science and Technology*, vol. 31, no. 3, p. 035023, 2016.
- [23] A. D. C. S. Baroni, S. De. Gironcoli, “Phonons and related crystal properties from density-functional perturbation theory,” *Reviews of Modern Physics*, vol. 73, pp. 515–562, 2001.
- [24] F. Giustino, M. L. Cohen, and S. G. Louie, “Electron-phonon interaction using wannier functions,” *Physical Review B*, vol. 76, no. 16, 2007.
- [25] C. Verdi and F. Giustino, “Frohlich electron-phonon vertex from first principles,” *Phys Rev Lett*, vol. 115, no. 17, p. 176401, 2015.
- [26] J. Noffsinger, F. Giustino, B. D. Malone, C.-H. Park, S. G. Louie, and M. L. Cohen, “EPW: A program for calculating the electron–phonon coupling using maximally localized wannier functions,” *Computer Physics Communications*, vol. 181, no. 12, pp. 2140–2148, 2010.
- [27] D. Rode, “Low-field electron transport,” *Semiconductors and semimetals*, vol. 10, pp. 1–89, 1975.
- [28] “MPI: A message-passing interface standard version 3.0,” 2012.
- [29] T. Kunikiyo, M. Takenaka, Y. Kamakura, M. Yamaji, H. Mizuno, M. Morifuji, K. Taniguchi, and C. Hamaguchi, “A monte carlo simulation of anisotropic electron transport in silicon including full band structure and anisotropic impact-ionization model,” *Journal of Applied Physics*, vol. 75, no. 1, p. 297, 1994.
- [30] M. Lundstrom, *Fundamentals of carrier transport*. Cambridge University Press, 2009.
- [31] A. Kokalj, “Computer graphics and graphical user interfaces as tools in simulations of matter at the atomic scale,” *Computational Materials Science*, vol. 28, no. 2, pp. 155–168, 2003.
- [32] J. P. Perdew and Y. Wang, “Accurate and simple analytic representation of the electron-gas correlation energy,” *Physical Review B*, vol. 45, no. 23, pp. 13 244–13 249, 1992.
- [33] P. Giannozzi, S. Baroni, N. Bonini, M. Calandra, R. Car, C. Cavazzoni, D. Ceresoli, G. L. Chiarotti, M. Cococcioni, I. Dabo, A. Dal Corso, S. de Gironcoli, S. Fabris, G. Fratesi, R. Gebauer, U. Gerstmann, C. Gougoussis, A. Kokalj, M. Lazzeri, L. Martin-Samos, N. Marzari, F. Mauri, R. Mazzarello, S. Paolini, A. Pasquarello, L. Paulatto, C. Sbraccia, S. Scandolo, G. Sclauzero, A. P. Seitsonen, A. Smogunov, P. Umari, and R. M. Wentzcovitch, “Quantum espresso: a modular and open-source software project

- for quantum simulations of materials,” *J Phys Condens Matter*, vol. 21, no. 39, p. 395502, 2009.
- [34] H. J. Monkhorst and J. D. Pack, “Special points for brillouin-zone integrations,” *Physical Review B*, vol. 13, no. 12, pp. 5188–5192, 1976.
- [35] A. A. Mostofi, J. R. Yates, Y.-S. Lee, I. Souza, D. Vanderbilt, and N. Marzari, “wannier90: A tool for obtaining maximally-localised wannier functions,” *Computer Physics Communications*, vol. 178, no. 9, pp. 685–699, 2008.
- [36] M. H. Wong, K. Sasaki, A. Kuramata, S. Yamakoshi, and M. Higashiwaki, “Electron channel mobility in silicon-doped Ga<sub>2</sub>O<sub>3</sub> mosfets with a resistive buffer layer,” *Japanese Journal of Applied Physics*, vol. 55, no. 12, p. 1202B9, 2016.
- [37] H. Peelaers and C. G. Van de Walle, “Brillouin zone and band structure of  $\beta$ -Ga<sub>2</sub>O<sub>3</sub>,” *physica status solidi (b)*, vol. 252, no. 4, pp. 828–832, 2015.
- [38] J. Kolnik, İ. H. Oğuzman, K. F. Brennan, R. Wang, P. P. Ruden, and Y. Wang, “Electronic transport studies of bulk zinblende and wurtzite phases of gan based on an ensemble monte carlo calculation including a full zone band structure,” *Journal of Applied Physics*, vol. 78, no. 2, pp. 1033–1038, 1995.